Tellus (2006), 58A, 236–253
Printed in Singapore. All rights reserved

TELLUS

Transition of a synoptic system to a polar low via interaction with the orography of Greenland

By REBEKAH MARTIN* and G. W. K. MOORE, *Department of Physics, University of Toronto, 60 St. George St., Toronto, Ontario, M5S 1A7 Canada*

(Manuscript received 27 January 2005; in final form 10 October 2005)

ABSTRACT

A case study of a polar low that occurred over the Labrador Sea from December 29–31, 1997 was performed using the Penn State–NCAR Mesoscale Model version 5 (MM5). The polar low was imaged by the synthetic aperture radar (SAR) on the RADARSAT-1 satellite and as a result, unique high resolution information on the polar low's surface expression is available. This low is also of interest as it formed from a synoptic-scale low pressure system that underwent a bifurcation through an interaction with the topography of Greenland. Our model results show that the polar low achieved a minimum central pressure of 954 hPa with maximum 10 m wind speeds in excess of 30 ms^{-1}. Coincident SSM/I data are in agreement with the model surface wind speed field. Sensitivity studies showed that the genesis of the low was relatively insensitive to air–sea fluxes of sensible and latent heat. The model precipitation field indicates the presence of features reminiscent of rainbands observed to occur in association with tropical cyclones, as well as frontal features typically seen in mid-latitude baroclinic systems. In addition, our model results indicate that precipitation as well as the surface wind contributes to the polar low's surface expression as imaged by SAR.

1. Introduction

Polar lows are mesoscale cyclones that occur primarily during winter months over high latitude oceans. Rasmussen and Turner (2003) defines a polar low as "a small, but fairly intense maritime cyclone that forms poleward of the main baroclinic zone (the polar front or other major baroclinic zone). The horizontal scale of the polar low is approximately between 200 and 1000 kilometres and surface winds near or above gale force." The existence of these small but intense weather systems over the Norwegian Sea has been known since the 1960s (Harley, 1960; Harrold and Browning, 1969), but it was not until the advent of satellite imagery that it became apparent that polar lows were, in fact, a global phenomenon occuring over open waters at high latitudes in both hemispheres (Rasmussen and Turner, 2003).

With surface winds that may be of hurricane strength, polar lows can present a serious threat to marine operations that happen to be in their path. These systems are understandably difficult to forecast, since their characteristic scale is at the limits of available resolution in global models, and they occur in data sparse regions. Regional models may capture the development of a polar low, but without correct initialization – which may be an issue in data sparse regions – they too may fail to forecast the development of a polar low. This lack of forecast skill associated with polar lows adds to their potential hazard to maritime traffic and operations (Rasmussen and Turner, 2003). Polar lows may also play an important role in the climate system as a result of the intense air–sea interaction that is associated with them and which may contribute to the process of deep ocean convection through the densification of surface waters (Moore et al., 1996; Marshall et al., 1998; Renfrew et al., 1999).

The Labrador Sea has only recently been identified as a region where polar lows occur (Mailhot et al., 1996; Moore et al., 1996; Rasmussen et al., 1996; Moore and Vachon, 2002; Moore and Vonder Haar, 2003). The area's remoteness and the resultant data void over the Labrador Sea and Davis Strait make the study of polar lows in this region particularly challenging. Consequently, satellite data must be primarily relied upon for information about Labrador Sea polar lows. There are, however, some limitations with existing operational satellite data such as visible or IR imagery that provide information only at cloud top and do not provide any information regarding the surface circulation. Passive microwave sounders have recently provided temperature data showing the warm cores of polar lows (Forsythe and Vonder Haar, 1996; Moore and Vonder Haar, 2003), but they provide a spatial resolution that is relatively coarse when compared to the scales of most polar lows.

It has been recently proposed that synthetic aperture radar (SAR) is a useful tool with which to investigate the surface

*Corresponding author.
e-mail: remartin@atmosp.physics.utoronto.ca

DOI: 10.1111/j.1600-0870.2005.00169.x

dynamics of maritime storms such as polar lows (Sikora et al., 2000; Moore and Vachon, 2002; Wu and Liu, 2003). RADARSAT-1 was launched by the Canadian Space Agency in 1994 and is a polar orbiting SAR instrument, capable of returning imagery with a swath width of about 500 km and resolution of 100 m in its ScanSAR mode of operation. The C-band frequency of RADARSAT-1 passes through heavy cloud cover and precipitation with little or no attenuation or scattering (Katsaros et al., 2000). At this wavelength, the microwave radiation is Bragg scattered off the surface of the ocean by capillary waves, which are forced by surface level winds (Mourad et al., 2000). As such, SAR provides unprecedented imagery of the signature of near surface winds over the surface of the ocean. In addition to information on the surface wind field associated with cyclones, SAR imagery also contains signatures associated with atmospheric processes such as convection and precipitation that leave a signature on the ocean's surface (Atlas and Black, 1994; Katsaros et al., 2000; Melsheimer et al., 2001).

Although Labrador Sea polar lows have been a fairly recent discovery, case studies have been done of these systems using both satellite data and numerical simulations. Rasmussen et al. (1996) made use of satellite imagery to compile an extensive climatology of polar low events over the Labrador Seas. This study concluded that most polar lows in the region form within a narrow latitude band centered on 58°N. In addition, they concluded that these lows typically have a long tail extending in an east-west direction, and occasionally will propagate toward Cape Farewell at the tip of Greenland. A prime example of this type of polar low was given as a case that occurred from January 11–12, 1989. This case has been studied both with satellite data products (Forsythe and Vonder Haar, 1996), and numerically (Mailhot et al., 1996). A case study of a February 1997 Labrador Sea polar low was detailed by Pagowski and Moore (2001). That study employed MM5 and a detailed analysis of the effect of the marginal ice zone on the evolution of the simulated boundary layer and polar low development was done.

In this paper, we study a Labrador Sea polar low that occurred in late December of 1997. There are several factors that made this case an attractive one for detailed analysis. First, the availability of the high resolution RADARSAT-1 SAR imagery of the low in its mature state provides an unprecedented view of the low's surface expression that can be used to both validate model results and investigate some of the system's smaller scale dynamics. Second, this low is of interest because of the synoptic environment that preceded and contributed to its genesis. Prior to the development of the polar low, a synoptic-scale cyclone had tracked northeastward from the Newfoundland coast and impinged upon the rather significant barrier to atmospheric flow that is Greenland's southern tip. Because of this interaction with Greenland's orography, the parent low was actually split into two closed surface lows to the east and west of Cape Farewell. The deeper low was found to the west of the island, and interaction with an upper level PV anomaly helped to spin the remnants up into a polar low (Moore and Vachon, 2002). Finally, the apparent retrograde propagation of the low toward the west and across the Davis Strait is of interest. Mean flow in the Labrador Sea region is northwesterly, however this particular polar low formed to the northwest of the parent synoptic system. This is then opposite to the mean flow direction, and the retrograde propagation is likely due to the significant orographic forcing in the region as well as the location of the sea ice edge and attendant baroclinic environment.

We present a high-resolution simulation of its development that was performed with the Penn State–NCAR Mesoscale Model version 5 (MM5) with boundary and initial conditions provided by the Canadian Meteorological Centre (CMC) regional analysis. The quality of the simulation will be assessed through a comparison with the RADARSAT-1 image of the surface wind associated with the polar low.

2. Synoptic background

On December 27, 1997, a synoptic-scale cyclone tracked into the North Atlantic from northern tip of Newfoundland. The sea-level pressure, 10 m wind and 2 m air temperature fields from the CMC regional analysis are shown in Fig. 1, with a resolution of 35 km over the region of interest. As the low tracked into the North Atlantic, it moved north eastwards toward the tip of Greenland, and deepened by approximately 26 hPa during the 24-h period from 0000 UTC December 27 to 0000 UTC December 28 (Fig. 1a–c). This system therefore met the requirements for being a meteorological "bomb" as defined by Sanders and Gyakum (1980). Around 0000 UTC on December 28, the circulation associated with the cyclone began to encounter the tip of Greenland, which has a height of over 2000 m within 200 km of the coast. The orography of the island presented a significant barrier to airflow, as can be seen in the elongation of the sea-level pressure contours in Fig. 1c and d. As a consequence of this interaction, the cyclone underwent a bifurcation with its associated lower level circulation actually splitting around the island (Moore and Vachon, 2002). At 1200 UTC on 28th (Fig. 1d), the larger part of the secondary circulation of the parent cyclone was found to the west of the island over the Labrador Sea and had a central pressure 975 hPa, while the smaller part of the circulation to the east of the island had a central pressure of about 980 hPa. A pre-existing warm surface pool (Fig. 1a), was trapped against the west coast of Greenland, and may have contributed to the cyclone's propagation toward the north and west. This warmer-mixed layer could have presented less of a barrier to mixing than the cold air over the ice to the east would have. By 0000 UTC on December 29, the cyclone had completely split at the surface (Fig. 1e). In addition, the segment on the western side of the island had begun to form into a mesoscale low along a low level cold front associated with the sea ice edge. Although the SLP fields from the CMC analysis would indicate that at this time

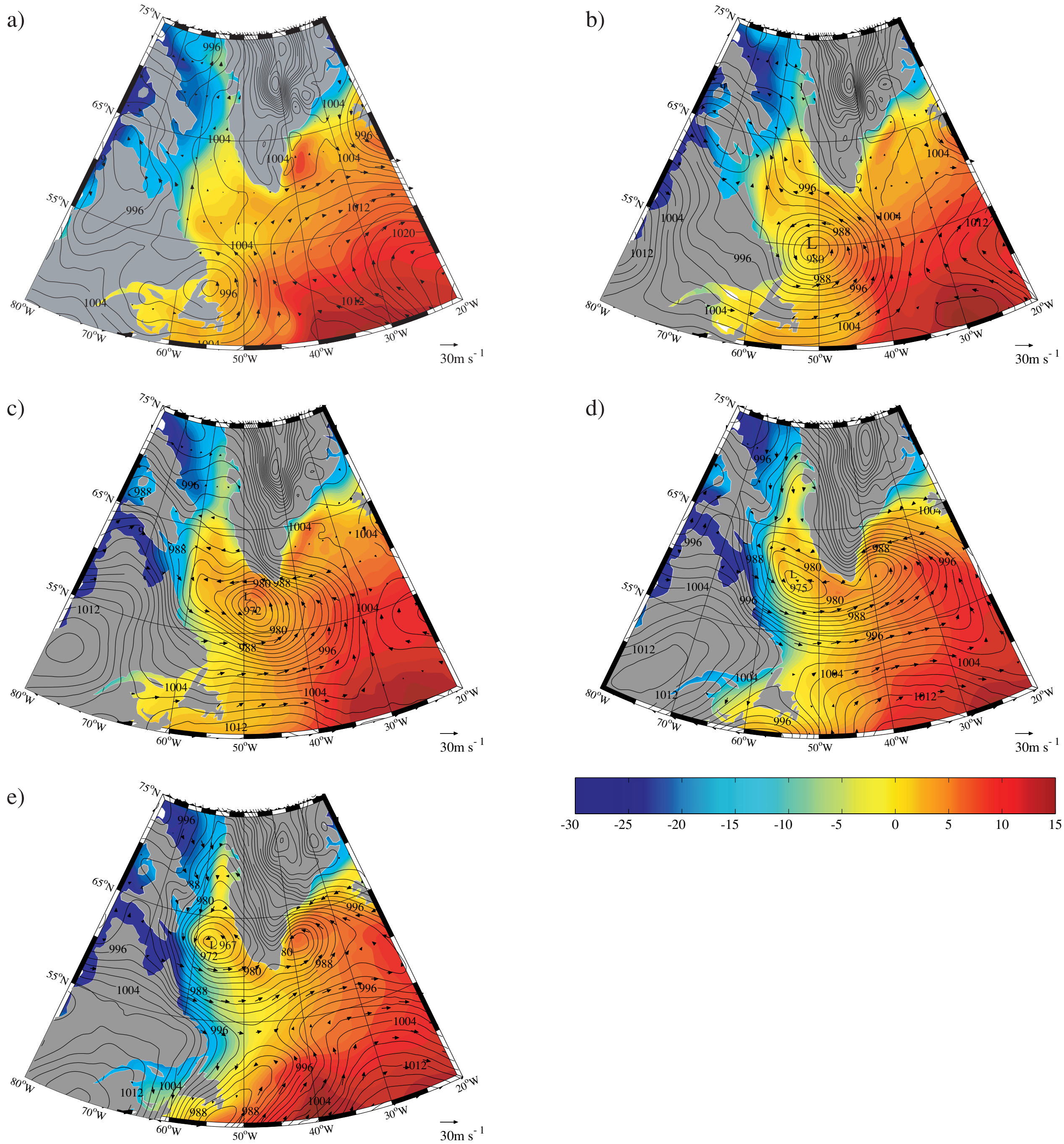

Fig 1. Sea-level pressure (contours, hPa), 2 m temperature (shading, °C) and 10 m wind vectors (ms^{-1}) from the Canadian Meteorological Centre's Regional Analysis for: (a) 0000 UTC December 27, 1997; (b) 1200 UTC December 27, 1997; (c) 0000 UTC December 28, 1997; (d) 1200 UTC December 28, 1997; and (e) 0000 UTC December 29, 1997.

the polar low has fully transitioned from the parent system, higher resolution simulations are able to show more detail and hence allow for a better idea of how this transition does occur.

Fig. 2 shows the 500 hPa geopotential height, temperature, and wind vectors also from the CMC analysis for 1200 UTC on December 28. Once the low had bifurcated around the island, an upper level circulation was present to the west of the island, and

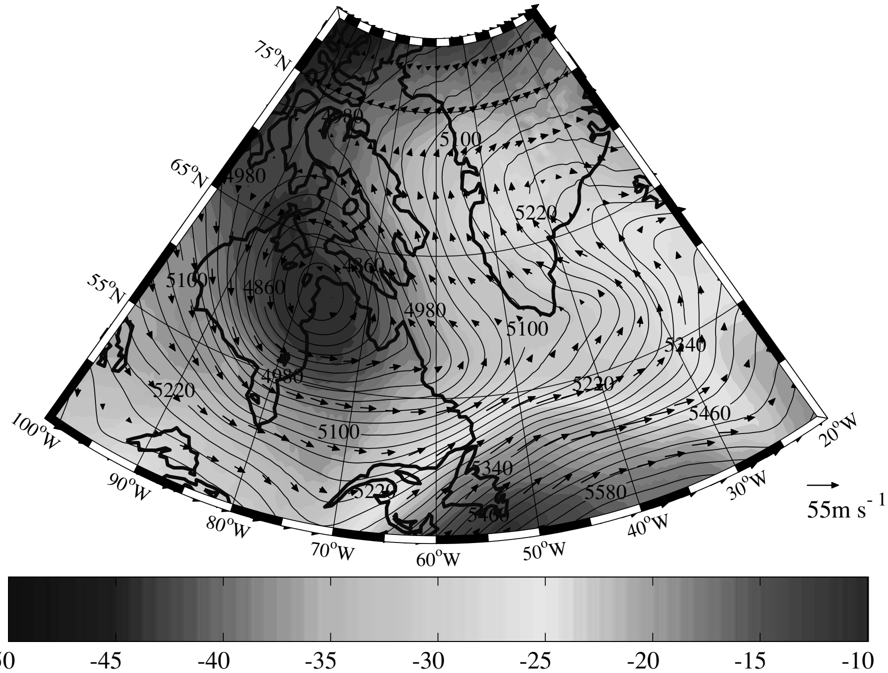

Fig 2. 500 hPa geopotential height (contours, m), 500 hPa temperature (shaded, °C), 500 hPa wind vectors for 1200 UTC December 28, 1997.

likely helped to generate the polar low as described by Moore and Vachon (2002). This upper level circulation and the previously mentioned low level baroclinicity in the form of a surface thermal gradient along the sea ice edge would have contributed to the growth of the low through the mechanism proposed by Hoskins et al. (1985). Additionally, the vorticity advected into the region by the parent low would have aided the communication between the upper level PV anomaly and the low-level baroclinic zone (Rasmussen and Turner, 2003).

Figure 3 shows AVHRR imagery of the evolution of the bifurcated cyclone into the polar low. In the image at 1947 UTC on December 28, 1997 (Fig. 3a), the secondary circulation center of the synoptic-scale low is noticeable as is the cloud-free region just north of 60°N to the west of Cape Farewell. High cloud is also seen over the Labrador Sea streaming off of Baffin Island, and cloud streets associated with cold continental air are seen in the south-west sector of the image streaming off of the northern coast of Labrador and through Hudson Strait. The image at 2106 UTC on December 20, 1997 (Fig. 3b) shows the polar low at a time close to its minimum central pressure (MCP) as shown by the CMC analysis. In this image, a well-defined, cloud-free eye is apparent, along with high cloud to the west and north of the low. Lower cloud to the east of the low is associated with the warmer air trapped against the coast of Greenland and exhibits cellular convection. To the south and west of the low, cloud streets continue to stream off the ice edge through Hudson strait, and indicate the presence of cold air. The image at 2044 UTC on December 30, 1997 (Fig. 3c) shows the movement of the polar low toward the west coast of Greenland and the clouds associated with the low are somewhat spiral in appearance.

Figure 4 shows the RADARSAT-1 image of the polar low at 2100 UTC on December 29, 1997. This time corresponds roughly to that of the AVHRR image in Fig. 3b. In the image, higher pixel brightnesses indicate greater backscatter and correspondingly higher surface wind speeds. Of particular note is the low wind speed eye, which is indicated by the dark region in the centre of the storm that can be seen to match the position of the cloud-free eye in the AVHRR imagery. The ice edge runs along the left-hand side of the image, and for our purposes indicates a region where the wind information is lost. Several small-scale wind features may be seen within the low, indicating some very fine structure that was present within the low. In addition, the asymmetry of the low, particularly in the region of the eye, may be seen. To the south-east of the eye, linear convection can be seen in the image in the lines of higher backscatter farther out from the high wind speed core of the low. To the east and north-east of the low, cellular convection is apparent in the mottled appearance of the image. This surface imagery mirrors and augments the cloud top imagery provided by the AVHRR images and clearly demonstrates the additional information that SAR can provide about marine weather systems.

Figure 5 shows the SSM/I wind speed retrieval at 2030 UTC on December 29, 1997. The low wind speed center of the low can be seen from this figure at 63.5°N and 58°W and corresponds well to the center of the low as imaged by RADARSAT-1 (Fig. 4). In addition, the SSM/I winds show the strongest winds to the south and west of the low, the region where the

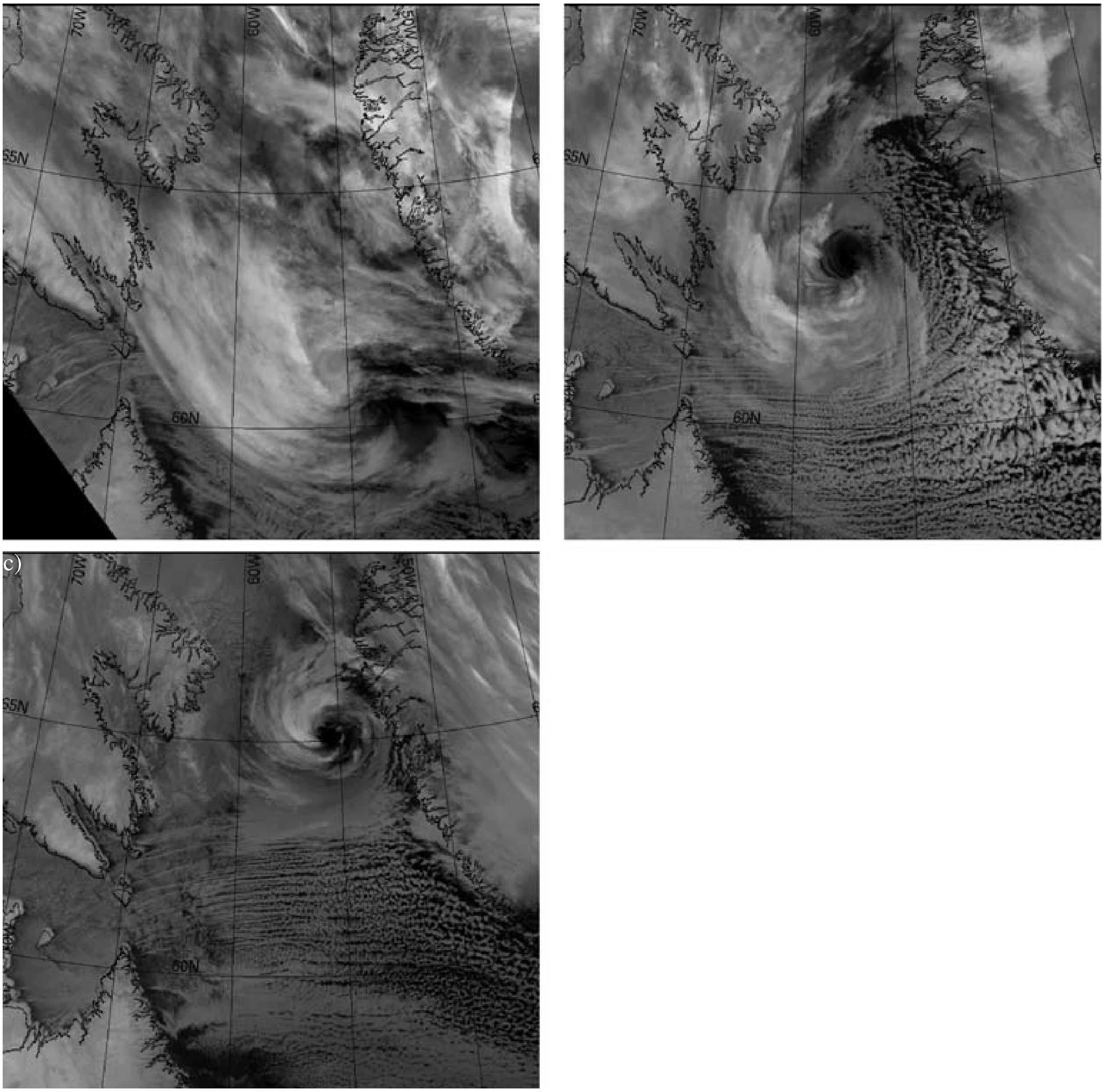

Fig 3. AVHRR images of the low over the Labrador Sea at: (a) 1947 UTC December 28, 1997; (b) 2106 UTC December 29, 1997; and (c) 2044 UTC December 30, 1997.

higher backscatter is seen in Fig. 4. However, a comparison of Figs. 4 and 5 clearly shows the impact that the higher resolution SAR imagery has information regarding the low's surface expression.

3. Methods

The Penn State–NCAR Mesoscale Model version 5 (MM5) version 3.6.1 was used to perform the case study simulations. The simulation runs were done on three nested domains at 27 km, 9 km, and 3 km horizontal resolutions, respectively. The outer 27 km domain had dimensions of 100 × 94 while the two inner domains had dimensions of 166 × 148 and 178 × 163, respectively. The three model domains used are shown in Fig. 6. The model was initialized using the CMC's regional analysis, examples of which were shown in Figs. 1 and 2. Model simulations were run with 40 vertical sigma levels, with 20 of these layers in the lower 2 km of the atmosphere where the average spacing was 100 m. The model top was set at 100 hPa, where a radiative boundary condition was applied.

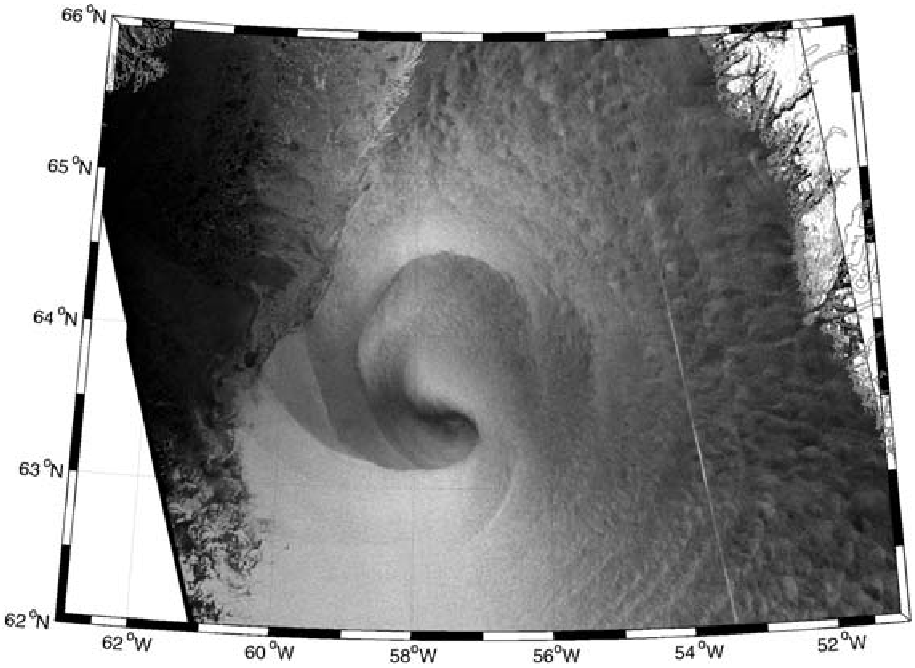

Fig 4. RADARSAT-1 SAR image of the polar low over the Labrador Sea at 2130 UTC December 29, 1997.

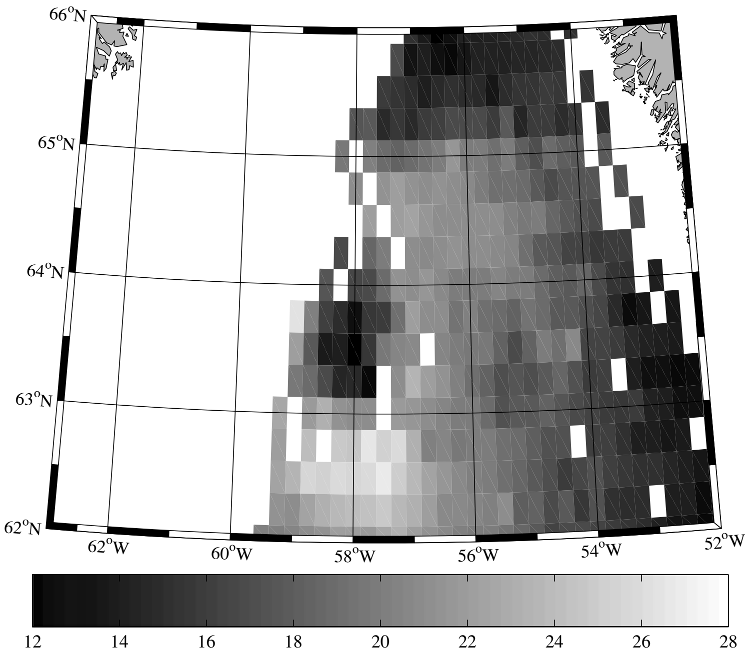

Fig 5. SSM/I wind speed retrieval (ms^{-1}) at 2030 UTC, December 29, 1997.

The Grell sub-grid cumulus convection parameterization (Grell et al., 1994) was applied on the outer 27 and 9 km domains with no cumulus parameterization in the inner 3 km domain. A simple ice microphysics scheme that is included in the standard distribution of the MM5 package and does not allow for supercooled water or graupel was applied on all domains. Two planetary boundary layer (PBL) parameterizations, namely the MRF (Hong and Pan, 1996) and the ETA (Janjic, 1990; Janjic, 1994), were employed in the sensitivity study simulations. The Polar MM5 modifications were used in conjunction with the simulations using the ETA PBL (Bromwich et al., 2001). The Polar MM5 allows for a fractional sea ice edge and seven soil layers instead of the standard five layers. As the simulation was done mostly over ocean, the inclusion of the marginal ice zone was of particular importance for the development of the low (Pagowski and Moore, 2001). In addition, the Garratt

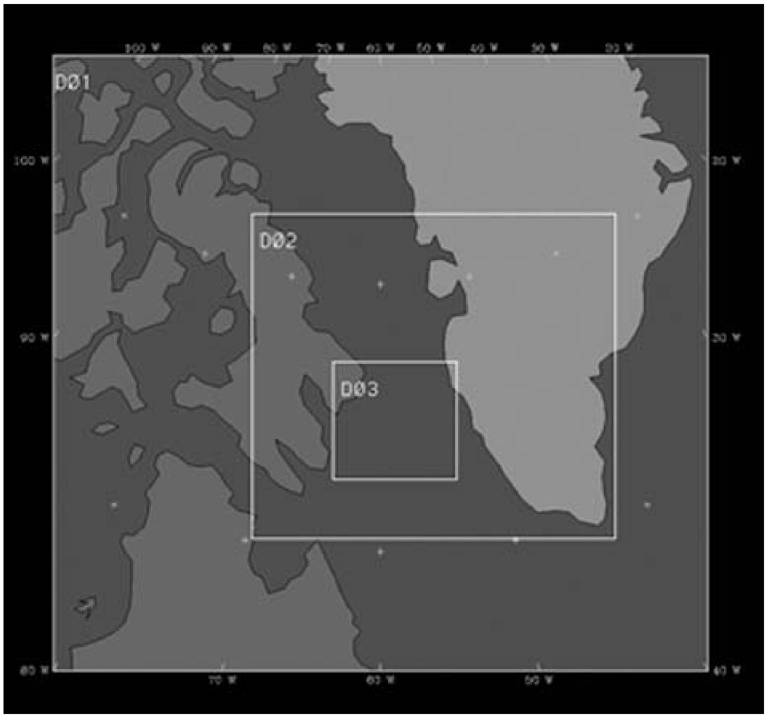

Fig 6. The three model domains used in this study.

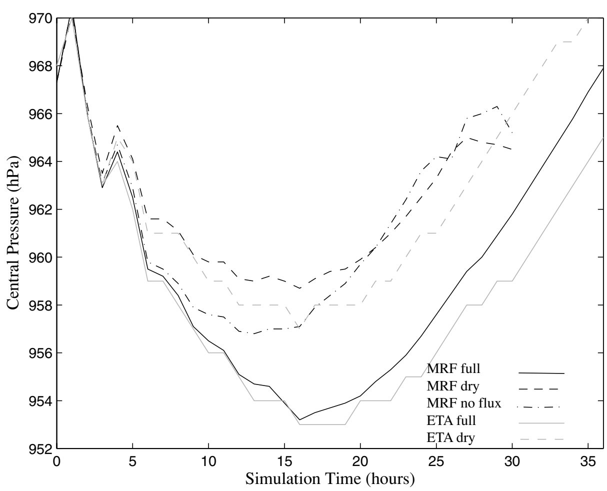

Fig 7. Time evolution of the MCP of the polar low over simulation time for different physics options as given by legend.

formulation for the roughness length was used as it has been previously shown (Pagowski and Moore, 2001) to give a more physical parameterization of air–sea heat moisture and momentum fluxes in the Labrador Sea region and is therefore an important ingredient for achieving a more realistic simulation.

The location of the ice edge was determined from the CMC analysis fields and, along with the sea surface temperature (SST), was held constant over the course of the simulation period. When the Polar MM5 modifications were used along with the MRF PBL a fractional sea ice profile was used, while in the experiments using the MRF PBL only a binary value of sea ice was allowed for, and the Polar MM5 could not be used.

All simulations were initialized at 0000 UTC on December 29, 1997 and were run for 36 h. This span of time covered the transition of the parent circulation that was birfurcated by the orography of Greenland to the polar low. In addition, the simulation period covered the eventual filling of the low and its movement away from the ice edge. Simulations were also done that were initialized up to 36 h before this time, however they were not found to significantly affect the dynamical development of the polar low. Consequently, 0000 UTC on December 29, 1997 was chosen as the initial time for the simulations as this time allowed for optimal study of the full life cycle of the low.

4. Polar low simulation

4.1. Sensitivity study

Figure 7 shows the time evolution of the central pressure of the low as found in sensitivity studies conducted under several different model configurations. Table 1 also summarizes the sensitivity experiments that were carried out. Two full physics simulations were run using both the ETA and the MRF PBL parameterizations. Dry simulations in which there was no latent heat release and no cumulus parameterization were also run with both of these schemes. Finally, simulations were run with the MRF PBL scheme in which surface heat fluxes were turned off. In the figure, black lines correspond to the MRF PBL simulations while gray lines correspond to the ETA PBL simulations. Solid lines correspond to full physics options, dashed lines correspond to

Table 1. Summary of sensitivity experiments

Experiment	Fluxes	Moist processes	MCP (hPa)
ETA full	Yes	Yes	953
MRF full	Yes	Yes	953
ETA dry	Yes	No	957
MRF dry	Yes	No	959
MRF no flux	No	Yes	957

MCP determined over the course of the simulation.

the dry runs, and the dash dotted line corresponds to the MRF PBL run with no fluxes. As previously mentioned, the ETA PBL studies employed the Polar MM5 modifications while the MRF PBL studies used the stock MM5 physics. This meant that ETA simulations had a marginal ice zone while MRF simulations did not. Surface heat fluxes from simulations with the ETA PBL parameterization have previously been shown to be biased high at high latitudes (Renfrew et al., 2002). The MRF PBL scheme has been shown to be a better choice over the Labrador Sea region because its surface fluxes agree better with observations than do the ETA fluxes (Pagowski and Moore, 2001). Sensitivity studies were conducted on only the two outer domains of the simulation.

From the sensitivity study (Fig. 7), it appears that during the first 24 h of the simulation the surface heat flux did not contribute significantly to the deepening of the polar low. This is shown in the similarity of the MCP trend lines of the ETA PBL, the MRF PBL, and the MRF no flux simulations, and is somewhat contrary to the situation found in other polar low case studies. For example, Bresch et al. (1997) found that turning off surface heat fluxes during the first 24 h of simulation could actually prevent the formation of a polar low. The behavior in this present case is possibly a consequence of the fact that the parent circulation advected a sufficient amount of moisture into the Labrador Sea area to fuel the development of the polar low. As a result, the genesis was not as dependent on the air–sea fluxes during its development stages as has been observed in other case studies. This scenario is supported by the fact that in the ETA and the MRF simulations, where the total turbulent heat flux can differ greatly, the depths of the simulated lows were identical up to the 12th hour of simulation time. The MRF no flux case achieved a MCP that was only 1 hPa greater than the other two in hour 12 of the simulation. However, after 12 h of simulation time it appears that the inclusion of fluxes became important, as it is at this point that the MRF no flux simulated low started to fill. The simulated low in this case ultimately filled more quickly than those in the other cases.

The two dry physics cases, ETA dry and MRF dry, achieved a MCP 4 hPa higher than that achieved in the full physics case. This indicates that moist processes and perhaps some condensational effects were important in helping the low to attain its eventual simulated depth. In both dry physics cases, the MCP is reached 17 h into the simulation, which was the same simulation time that the MCP was reached in the two full physics cases. The general trend of the simulated low to fill appears to be comparable between the two full physics cases and the two dry physics cases. From this, we would conclude that surface flux processes were important in maintaining the low's strength after it had reached maturity. This is probable, because at maturity the system had used the energy provided by the advected moisture from the parent circulation. As the low was filling, it was actually tracking into areas of higher surface fluxes to the west and north of its maximum strength positioning. As a result, the low was able to maintain itself longer than it might otherwise have done.

4.2. *Surface evolution*

Given the results of the sensitivity study, the simulations that we will describe below used the MRF PBL parameterization scheme. Figure 8 shows the sea-level pressure, 10 m wind vectors, and 2 m temperature on the inner 3 km domain for selected times during the simulation. At 0600 UTC on December 29 (Fig. 8a), the 2 m temperature field shows the pre-existing warm pool in the eastern part of the domain that is trapped against the west coast of Greenland. It can be seen from Fig. 1 that this warmer air was associated with the circulation of the parent synoptic low. The relatively warm 2 m air temperatures of 0°C in this area was quite striking, as is the fact that the 10 m winds are southerly, and hence they are retrograde to the mean winds in the region, which are northerly. This southerly flow trapped against the high topography of West Greenland, located just to the east of the model domain, is most likely an example of barrier flow (Parish, 1983; van den Broeke and Gallee, 1996; King and Turner, 1997). To the west, significantly colder air of −15°C is associated with strong northerly flow around Baffin Island and over the sea ice. The northerly flow was also most likely the result of barrier flow associated with the high topography of Baffin Island, seen at the very northwestern part of the domain. In this region, Baffin Island has topography in excess of 1500 m high, and so presents a significant barrier to the low level flow. The coldest air was located to the south of the low as was the region of highest surface wind speeds. This colder air can be seen to wrap around the low through the course of the simulation, and actually force the warmer air farther north isolating the warm core of the polar low.

At 0600 UTC on December 29 (Fig. 8a), the low had deepened to 960 hPa from its depth of 972 hPa at 0000 UTC on the 29th. Six hours later, as seen in Fig. 8b, the circulation had become more compact as the warmer air at the centre of the low was becoming sequestered, and the central pressure had dropped an additional 5 hPa. The system also displayed a high degree of asymmetry, as it did 6 h earlier, and at the start of the simulation. Fronts can be seen to the east and north of the low. Eighteen hours into the simulation at 1800 UTC on the 29th (Fig. 8c), the low achieved its MCP of 954 hPa. At that time, the low was occluded,

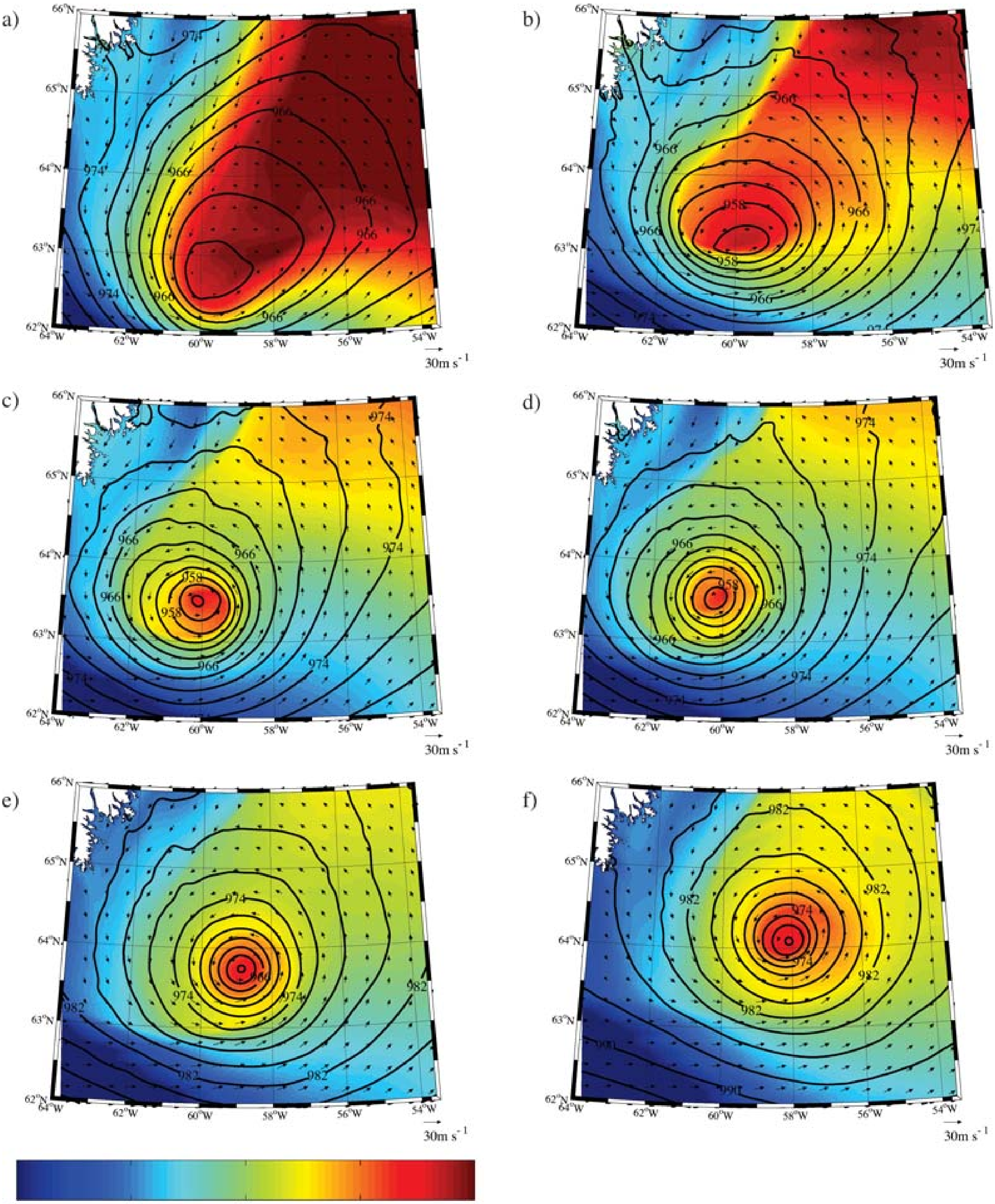

Fig 8. Model output on 3 km domain of sea-level pressure (contours, hPa), 2 m temperature (shaded, °C), and 10 m wind vectors (ms^{-1}) for: (a) 0600 UTC December 29, 1997; (b) 1200 UTC December 29, 1997; (c) 1800 UTC December 29, 1997; (d) 2100 UTC December 29, 1997; (e) 0600 UTC December 30, 1997; and (f) 1200 UTC December 30, 1997.

with a warm core at a temperature of -2°C, and surrounding air temperatures approximately 5°C colder.

Subsequent surface output shown in Fig. 8d–f shows that the low maintained its warm core for the remaining 18 h of the simulation. The latter half of the simulation showed that the polar low moved eastward while it was filling, moving toward the west coast of Greenland. This propagation is consistent with the AVHRR image shown in Fig. 3c.

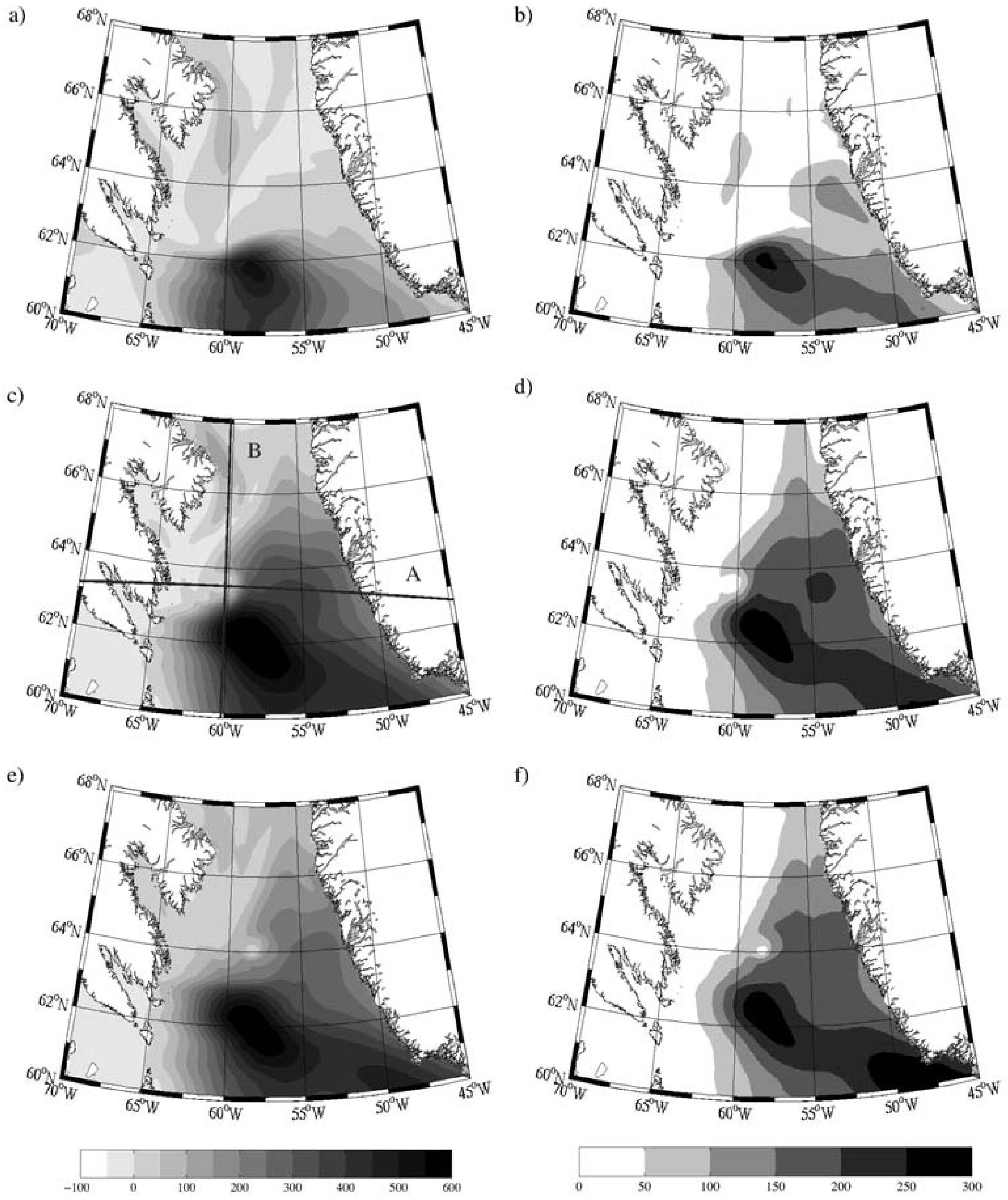

Fig 9. Model surface fluxes on the 9 km domain (Wm^{-2}): (a) sensible heat flux at 0600 UTC December 29, 1997; (b) latent heat flux at the same time as (a); (c) sensible heat flux at 2100 UTC December 29, 1997; (d) latent heat flux at the same time as (c); (e) sensible heat flux at 1200 UTC December 30, 1997; and (f) latent heat flux at the same time as (e). The lines on (c) indicate cross sections shown in Figure 11.

Figure 9 shows the simulated surface sensible and latent heat fluxes, and the sea-level pressure field for representative times in the simulation on the 9 km domain. As is typical over the Labrador Sea during the winter, the sensible heat fluxes are larger by a factor of approximately 2 as compared to the latent heat fluxes (Pagowski and Moore, 2001; Renfrew et al., 2002). Figure 9a and b shows the sensible and latent heat fluxes, respectively, for 0600 UTC on December 29, 1997. Here, the largest fluxes are actually located to the rear of the low, and so might not be expected to contribute as much to the development of the low, as was found in previous studies (Kuo and Reed, 1988; Kuo et al., 1991). Figure 9c and d shows the sensible and latent heat fluxes, respectively, for 2100 UTC on December 29, 1997, at the time of the available RADARSAT-1 image. At this time, the fluxes had strengthened considerably with peak values, in excess of 500 and 250 Wm^{-2} for the sensible and latent heat, respectively, occurring to the south and east of the low where the cold arctic air first comes into contact with the relatively warm surface waters of the Labrador Sea. However, at this time the fluxes are also high to the east of the low. Examination of the surface air temperature field at this time (Fig. 8) indicates that the advection of this cold arctic air by the polar low has reached this region. Figure 9e and f shows the sensible and latent heat fluxes, respectively, for 1200 UTC on December 30, 1997, which was the final simulation output time. Here the polar low has tracked eastward toward the west coast of Greenland into the region where elevated air–sea heat fluxes had occurred during the previous 18 h. The destabilization of the lower atmosphere by this surface heating most likely contributed to the maintenance of the polar low.

4.3. Model precipitation

Figure 10 shows the precipitation field on the 9 km domain at representative times during the simulation. Maximum

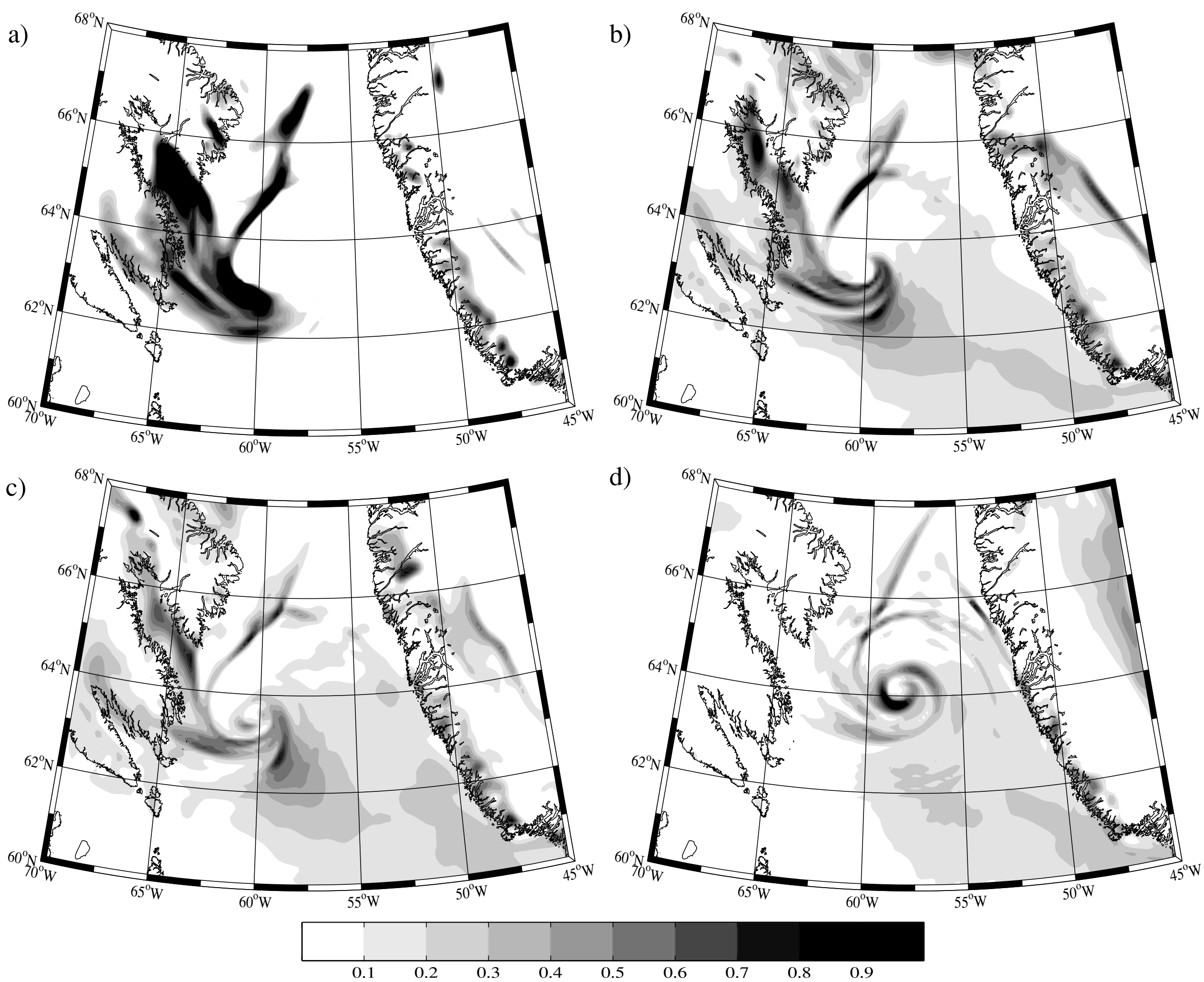

Fig 10. Model precipitation rates (mm h^{-1}, colored contours) on the 9 km domain for: (a) 1200 UTC December 29, 1997; (b) 1800 UTC December 29, 1997; (c) 2100 UTC December 29, 1997; and (d) 1200 UTC December 30, 1997.

precipitation rates are on the order of 4 mm h^{-1} up to hour 15 of the simulation, and are subsequently between 1–2 mm h^{-1}. At 1200 UTC on December 29, 1997 (Fig. 10a), precipitation along the ice edge front to the north of the developing low is a prominent feature. At this time there was also significant precipitation seen along Baffin Island's Cumberland Sound at the western edge of the domain, and this was probably due to orographically induced convergence. Figure 10b, 1800 UTC on the 29th, shows a maximum in precipitation both along the northern front and at the system center. In addition, some evidence of spiral banding can be seen in the precipitation field, although the low has not yet reached maturity. Figure 10c shows the precipitation field at 2100 UTC on December 29. Spiral bands have formed at this time and the orographic precipitation in Cumberland Sound has tailed off. Figure 10d shows the precipitation field for the final hour of the simulation at 1200 UTC on December 30, and the spiral bands surrounding the low center associated are particularly striking.

Figure 11 shows the precipitation field on the 3 km domain for 2100 UTC on December 29 and 1200 UTC on December 30. Figure 11a shows more detail of the model precipitation structure at the time that SAR imagery of the polar low was available (Fig. 4) than that shown in Fig. 10c. Figure 11b shows the spiral structure of the precipitation field that formed during the latter stages of the polar low's life cycle. It is interesting to note that these spiral bands are to the south of the low, rather than to the north, and this is another reflection of the fact that the warmer air in the system was actually located to the north and east of the low (Figs. 1 and 8). Additionally, the spiral bands are reminiscent of the rainbands associated with tropical systems, although there is unfortunately no way to confirm the existence of these bands with existing data.

The precipitation maximum corresponding to the front to the north of the polar low was a persistent feature throughout this course of the simulation. An examination of the surface streamfunction from the model output (not shown) indicates that the banded precipitation features are associated with convergence in the low-level wind field. This precipitation seems to be much like that reported in Bresch et al. (1997), who also reported mesoscale precipitation bands in their case study of a polar low over the Bering Sea.

4.4. *Cross section through the low*

In Fig. 12, the north-south and east-west cross sections indicated on Fig. 9d through the polar low at 3 and 2100 UTC on December 29, 1997 are shown. Cross sections were taken on model grid coordinates and consequently were not strictly meridional or zonal because of the mapping to polar stereographic projection. The fields presented in the cross sections are the potential temperature and the normal component of the wind.

Figure 12a shows the east-west cross section taken at 0300 UTC on December 29, 1997 across line "A" as labeled in Fig. 9d. At this time, the low level front along the ice edge could be seen in the western segment of the cross section. This low-level baroclinic zone can be likened to a low-level PV anomaly, as mentioned in Hoskins et al. (1985). The air behind this front was associated with strong northerly flow. To the east, away from the front and closer to the east coast of Greenland, the flow moves to be weakly southerly, and the potential temperature contours

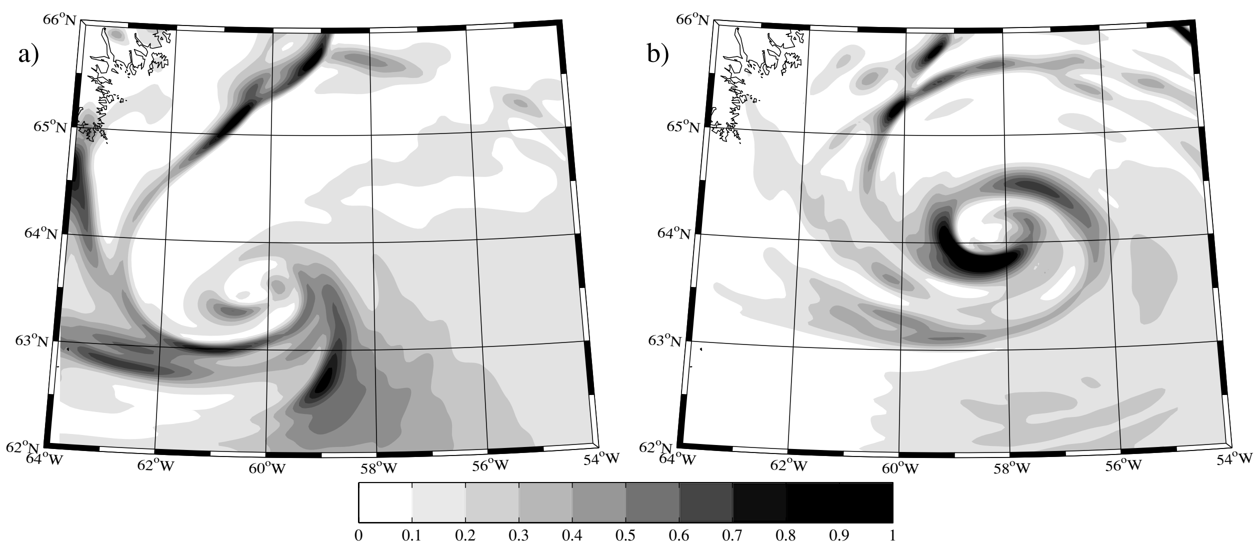

Fig 11. Model precipitation rates (mm h^{-1}, colored contours) on the 3 km domain for: (a) 2100 UTC December 29, 1997; and (b) 1200 UTC December 30, 1997.

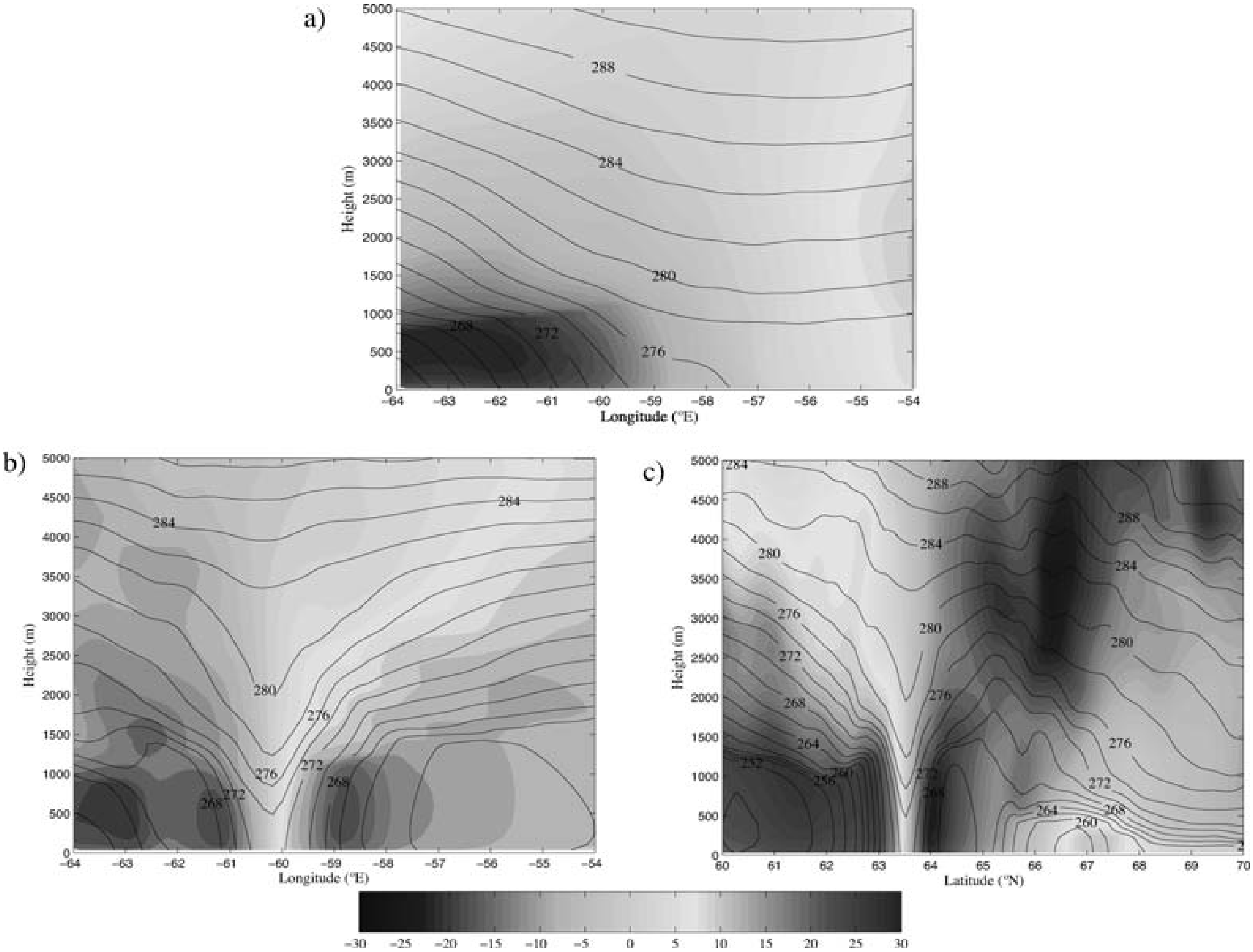

Fig 12. Model cross sections across the 9 km domain. (a) Height versus longitude east-west cross section of potential temperature (K, contours) and model u-wind (ms^{-1}, shaded) at 0300 UTC December 29, 1997. (b) Height versus longitude east-west cross section of potential temperature (K, contours) and model u-wind (ms^{-1}, shaded) at 2100 UTC. (c) Height versus latitude north-south cross section of potential temperature (K, contours) and model u-wind (ms^{-1}, shaded) at 2100 UTC.

indicated that there was a mixed layer in the lower 1000 m of the troposphere capped by fairly stratified air above.

Both cross sections of the mature low shown in Fig. 12b and c indicates that the polar low was a relatively shallow disturbance with a warm core. The east-west cross section labeled as "A" in Fig. 9d is given in Fig. 12b and shows cyclonic flow with wind speeds on the order of 20 ms^{-1} occurring at a height of approximately 500 m asl that were associated with the polar low. A separate maximum in wind speed on the order of 18 ms^{-1} occurred to the west of the vortex core near 63°W. This maximum is associated with the low level front along the ice edge and the presence of barrier flow along the coast of Baffin Island. The potential temperature contours indicate that the region to the east of the low was weakly stratified up to a height of about 1500 m, however, the contours also indicate that the warm core of the low extended to 4 km asl. The region of low stratification corresponds to the region of enhanced surface heating noted previously in Fig. 9.

The corresponding north-south cross section labeled as "B" in Fig. 9d is shown in Fig. 12c and indicates that the highest wind speeds—in excess of 26 ms^{-1}—occurred to the south of the low, and were associated with very cold arctic air. The two cross sections highlight the asymmetry of the low as seen in the RADARSAT-1 imagery (Fig. 4) where the strongest winds seem to be to the south of the low. The vortex core is more compact in the north-south direction, and, as mentioned above, the coldest air is found to the south of the low.

4.5. *Comments on genesis mechanisms*

The development of Labrador Sea polar lows is typically thought to be due to the interaction of an upper level potential vorticity anomaly with a shallow baroclinic zone that often develops along the ice edge in the Labrador Sea (Mailhot et al., 1996; Moore et al., 1996; Rasmussen and Turner, 2003). In the case discussed here, the upper level PV anomaly was certainly present as indicated by Fig. 2, and as shown by Fig. 2 of Moore and Vachon (2002), which showed PV on the 310 K surface from the NCEP reanalysis. From these two sources, the extent of the upper level anomaly can be seen to be about 1000 km in length scale along the longest axis. A low level potential vorticity anomaly was present along the ice edge in the region that the low formed in as indicated by the discussion of Fig. 12a. The penetration depth in the region that the low formed was calculated to be 7 km based on an average Brunt-Väisälä frequency in the upper stratified region of 0.02 s^{-1}, and the length scale of the upper level anomaly. The further modification of the penetration depth caused by the additional relative vorticity of the parent cyclone could double the penetration depth of the lone upper level anomaly. Certainly, based on the strength of the upper level anomaly and the initial cross section across the Labrador Sea, it is plausible to suggest that this polar low event was the result of an interaction between the upper level PV anomaly, the lower level ice edge baroclinic zone, and the additional vorticity provided by the parent circulation. This is further confirmed by the results of the sensitivity study which indicate that it is dynamical rather than moist processes that were most important to the development of this polar low, as in the absence of moist processes, the low is still able to develop with some significant strength.

5. Validation with the satellite imagery

As previously mentioned, there is a lack of ground-based observations available in the Labrador Sea region. Consequently, satellite imagery and analysis is crucial for validation of the simulation of this polar low. Specifically, AVHRR imagery (Fig. 3) and SAR imagery from RADARSAT-1 (Fig. 4), as well as SSM/I surface wind speed retrievals (Fig. 5) will be used to diagnose the success of the simulation.

A comparison of the available satellite imagery from 2100 UTC on December 29, 1997 (Figs. 3b and 4) shows that the positioning of the low in the simulation is too far to the west by 3° of longitude, but matches well in north-south positioning. This error in the position could possibly be due to incorrect time phasing of the simulation or problems with the initialization. Bresch et al. (1997) found similar errors in the positioning of their simulated low, and found that initialization of the simulation further into the development of the low resulted in better positioning of the storm. However, this simulation was initialized relatively close to the genesis of the low, and so the positioning error is likely due to a lack of observation over the Labrador Sea.

Figure 13 shows model derived cloud top temperatures, which correspond to the AVHRR IR imagery that is shown in Fig. 3b. The cloud top temperature was calculated using the RIP graphics package available with MM5 and based on absorption cross sections from Dudhia (1989). The cloud-free eye of the low is well captured in this figure as is the high cloud in the north and west sectors of the image. In addition, the lower level convective

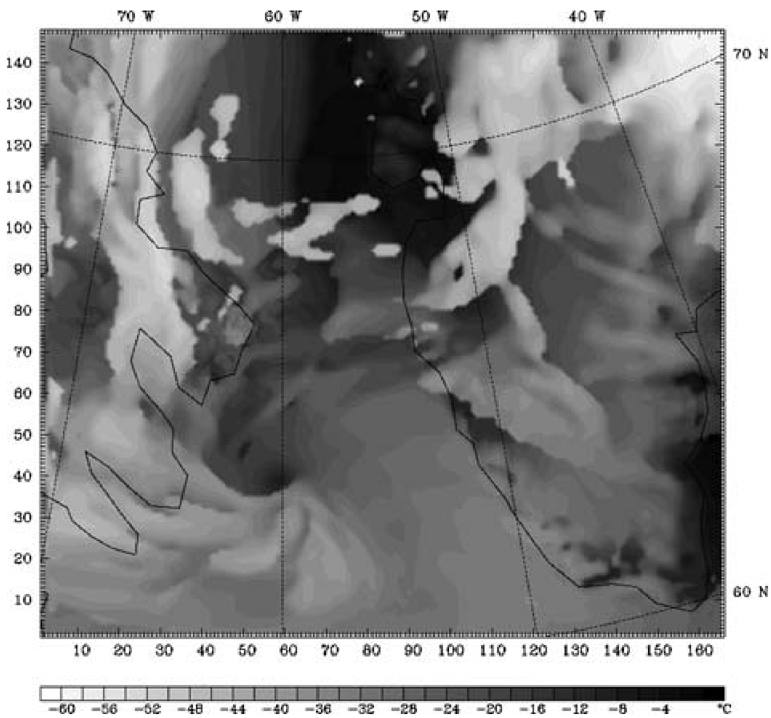

Fig 13. Cloud top temperature (K) derived from model fields.

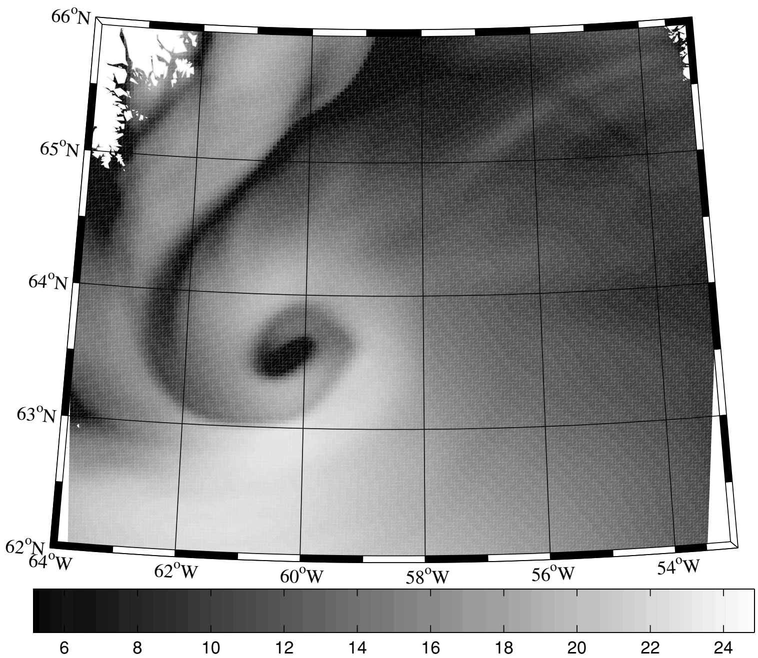

Fig 14. Model 10 m wind speed field on the 3 km domain for 2100 UTC December 29, 1997.

clouds to the south and east of the polar low seem to be relatively well resolved when compared to the AVHRR imagery.

Figure 14 shows the model derived 10 m wind speed for 2100 UTC on December 29, 1997. A gray-scale color mapping was used to facilitate comparison with the SAR and SSM/I data shown in Figs. 4 and 5. It should be noted that the SAR image provides information on wind speed only over the open water, and as a result, the comparison between Figs. 4 and 14 is only valid over the open ocean. Notwithstanding this caveat, there is a striking resemblance between the two. Of particular note is the presence of the low wind speed eye in both the model output and the SAR image. There is a striking discontinuity in wind speed present in the model output that spirals out of the low's center that is similar to the discontinuity present in the SAT image. In addition, both the model output and the SAR image indicate that the highest wind speeds occur to the south and west of the low. The retrieved maximum SSM/I winds as shown in Fig. 5 are higher than the 10 m model winds shown in Fig. 14; however, the maximum values agree to within 2 ms^{-1}.

Figure 15 provides a higher resolution view of the center of the polar low as imaged from RADARSAT-1. The low wind speed in the eye is clearly visible as well as multiple discontinuities in backscatter to its south and west. These latter features are most likely the result of changes in wind direction as well as wind speed that occur in this region (Fig. 8). In Fig. 16, which provides a closeup of the SAR image to the north of the low, small-scale beaded features can be seen along the primary discontinuity. Similar features have been observed in other SAR images of precipitating systems and have been attributed to the presence of surface wind speed variations associated with the associated vertical motion field as well as the damping effect that precipitation has on the surface roughness (Atlas, 1994; Jameson et al., 1997; Melsheimer et al., 2001). For low precipitation rates, the former is thought to be the dominant mechanism. In this regard, we note the primary discontinuity appears to be aligned in the model simulation with one of the banded precipitation features present at the time of the SAR image (Fig. 11a).

The regular spacing of the beaded features along with this frontal feature is reminiscent of what is observed to occur along narrow cold frontal rainbands in mid-latitude cyclonic storms

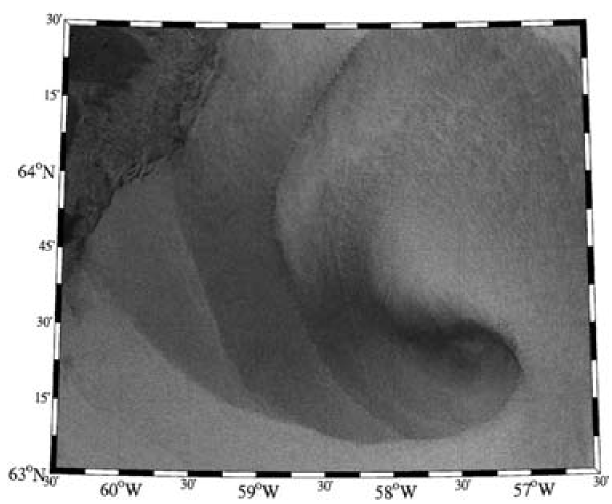

Fig 15. Closeup of the structure of the eye of the polar low in the RADARSAT-1 image from 2100 UTC December 29, 1997.

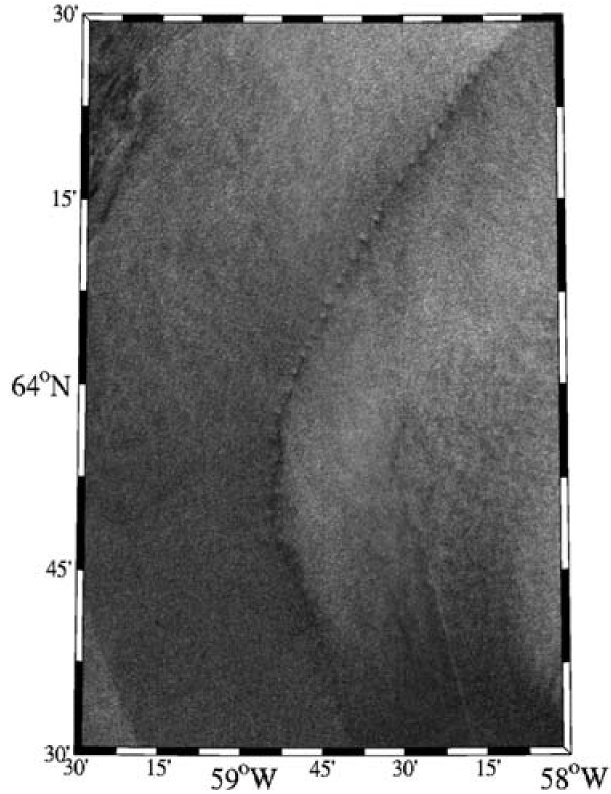

Fig 16. A closeup of the RADARSAT-1 image to the north of the low showing beading along the front.

(Hobbs, 1978; Wakimoto and Bosart, 2000). Theoretical explanations for the regular spacing of these features include instability due to horizontal shear in wind field (Hobbs and Persson, 1982; Moore, 1985). This appears to be consistent with the discontinuity in wind field seen in the model output (Fig. 14) as well as in the SAR image (Figs. 4 and 15).

6. Summary and discussion

A case of polar low genesis in the Labrador Sea has been investigated with a mesoscale forecast model. The polar low formed over the Labrador Sea out of the remnants of a synoptic-scale cyclone that had undergone a bifurcation through orographic interaction with the high topography of southern Greenland. The low formed in the region of the ice edge off Baffin Island, and was akin to mid-latitude marine cyclogenesis in that an upper level trough was present to the south-west of the genesis region. The ice edge provided a low-level baroclinic zone, and coupling between the lower and upper level anomalies may have been enhanced by relative vorticity provided by the parent cyclone (Hoskins et al., 1985; Rasmussen and Turner, 2003).

Although there was a lack of ground-based observations for the region, satellite imagery was available and provided a means of verification. Most notably, the RADARSAT-1 instrument provided resolution on the order of 100 m of the surface expression of the low, most notably its wind field. Sensitivity studies of the storm's development showed that surface fluxes were of little import to the deepening phase of the storm. This is in line with similar numerical experiments performed by Kuo and Reed (1988) for a synoptic-scale marine cyclone, but it is not entirely in line with the numerical simulation of a polar low in the Bering Sea performed by Bresch et al. (1997). In that study, suppression of the surface heat fluxes resulted in no polar low development. One of the major differences between that case study and the present one may be the presence of the parent cyclone and the orographic interaction in the Labrador Sea. It may be that the moisture advected into the region with the parent cyclone was sufficient to provide the fuel for the deepening seen in the first 24 h of the simulation, and so surface fluxes were less important until the provided energy had been converted. At any rate, dry baroclinic processes were significant to the development of this polar low, as one might expect. Both the sensitivity studies and the full physics model results indicate that while surface fluxes were not important to the development of the polar low, they were quite important to the longevity of the low. The surface heating provided by the region of elevated surface fluxes to the east of the low served to create a reservoir of air with low static stability, and hence aided in the maintenance of the low.

The model precipitation field was also found to be quite striking. Early in the development of the low, precipitation features were largely frontal in nature, and in particular the frontal precipitation associated with the wind discontinuity to the north of the low was a persistent feature throughout the simulated lifetime of the low. Latter times in the simulation of the low show spiral structures in the precipitation field and their existence appears to be confirmed by the available RADARSAT-1 image.

Positioning of the low in the simulation differs by 3° of longitude to the west of the position of the low as imaged by the AVHRR and SAR instruments. However, many other mesoscale dynamical features of the low that can be seen in the satellite imagery are manifest in the simulation. The correspondence between the simulated 10 m wind speeds and the RADARSAT-1 image is striking and in particular the low wind speed eye and the appearance of the discontinuity that spirals out of the low to the north that is present in both simulation and image is striking. The beaded features seen in the closeup of the RADARSAT-1 image of the low are remarkable, and although they are not apparent in the simulation, there is some evidence of beading along the front in the simulation from a plot of the streamfunction.

An interesting case of a polar low over the Labrador Sea has been studied in which surface fluxes were perhaps not so important to the genesis of the low due to the strength of the parent synoptic system. However, surface fluxes were shown to be important to determining the length of the life cycle of the low, and moist processes were important for determining the maximum strength of the low. It was also seen that both the wind field and the precipitation fields are consistent with the available SAR imagery of the polar low. This study has shown that further studies of polar lows in particular, and maritime storm systems in general in conjunction with SAR imagery should be illuminative of the very fine scale surface features of these systems.

7. Acknowledgments

The authors would like to thank S. Gravel for kindly providing the CMC analyses used in this paper, P. Vachon for assistance in the interpretation of the SAR image and M. Stastna for many helpful comments during the course of the research. The authors thank the Editor and Reviewers for comments that improved the manuscript. Funding for this research was provided by the Natural Sciences and Research Council of Canada and the Canadian Space Agency.

References

Atlas, D. 1994. Footprints of storms on the sea – a view from spaceborne synthetic-aperture radar. *J. Geophys. Res. Oceans* **99**, 7961–7969.

Atlas, D. and Black, P. G. 1994. The evolution of convective storms from their footprints on the sea as viewed by synthetic-aperture radar from space. *Bull. Am. Meteorol. Soc.* **75**, 1183–1199.

Bresch, J. F., Reed, R. J. and Albright, M. D. 1997. A polar-low development over the Bering Sea: analysis, numerical simulation, and sensitivity experiments. *Mon. Weather Rev.* **125**, 3109–3130.

Bromwich, D. H., Cassano, J. J., Klein, T., Heinemann, G., Hines, K. M. and co-authors. 2001. Mesoscale modeling of katabatic winds over Greenland with the Polar MM5. *Mon. Weather Rev.* **129**, 2290–2309.

Dudhia, J. 1989. Numerical study of convection observed during the winter monsoon experiment using a mesoscale two-dimensional model. *J. Atmos. Sci.* **46**, 3077–3107.

Forsythe, J. M. and Vonder Haar, T. H. 1996. A warm core in a polar low observed with a satellite microwave sounding unit. *Tellus A* **48A**, 193–208.

Grell, G. A., Dudhia, J. and Stauffer, D. R. 1994. *A Description of the Fifth-Generation Penn State/NCAR Mesoscale Model (MM5)*. NCAR, Boulder, CO, USA. pp. 122.

Harley, D. G. 1960. Frontal contour analysis of a 'polar low'. *Meteorol. Mag.* **89**, 146–147.

Harrold, T. W. and Browning, K. A. 1969. Polar low as a baroclinic disturbance. *Q. J. R. Meteorol. Soc.* **95**, 710–723.

Hobbs, P. V. 1978. Organization and structure of clouds and precipitation on mesoscale and microscale in cyclonic storms. *Rev. Geophys.* **16**, 741–755.

Hobbs, P. V. and Persson, P. O. G. 1982. The mesoscale and microscale structure and organization of clouds and precipitation in mid-latitude cyclones.5. The substructure of narrow cold-frontal rainbands. *J. Atmos. Sci.* **39**, 280–295.

Hong, S. -Y. and Pan, H. -L. 1996. Nonlocal boundary layer vertical diffusion in a medium-range forecast model. *Mon. Weather Rev.* **124**, 2322–2339.

Hoskins, B. J., Mcintyre, M. E. and Robertson, A. W. 1985. On the use and significance of isentropic potential vorticity maps. *Q. J. R. Meteorol. Soc.* **111**, 877–946.

Jameson, A. R., Li, F. K., Durden, S. L., Haddad, Z. S., Holt, B. M. and co-authors. 1997. SIR-C/X-SAR observations of rain storms. *Remote Sens. Environ.* **59**, 267–279.

Janjic, Z. I. 1990. The step-mountain coordinate: physical package. *Mon. Wea. Rev.* **118**, 1429–1443.

Janjic, Z. I. 1994. The step-mountain eta coordinate model: further development of the convection, viscous sublayer, and turbulent closure schemes. *Mon. Weather Rev.* **122**, 927–945.

Katsaros, K. B., Vachon, P. W., Black, P. G., Dodge, P. P. and Uhlhorn, E. W. 2000. Wind fields from SAR: could they improve our understanding of storm dynamics. *J. Hopkins APL Tech. D.* **21**, 86–93.

King, J. C. and Turner, J. 1997. *Antarctic Meteorology and Climatology. Cambridge Atmospheric and Space Science Series* Volume xi. Cambridge University Press, Cambridge, UK. pp. 409.

Kuo, Y. H. and Reed, R. J. 1988. Numerical-simulation of an explosively deepening cyclone in the eastern pacific. *Mon. Weather Rev.* **116**, 2081–2105.

Kuo, Y. H., Reed, R. J. and Lownam, S. 1991. Effects of surface-energy fluxes during the early development and rapid intensification stages of 7 explosive cyclones in the western Atlantic. *Mon. Weather Rev.* **119**, 457–476.

Mailhot, J., Hanley, D., Bilodeau, B. and Hertzman, O. 1996. A numerical case study of a polar low in the Labrador Sea. *Tellus A* **48A**, 383–402.

Marshall, J., Dobson, F., Moore, K., Rhines, P., Visbeck, M. and co-authors. 1998. The Labrador Sea deep convection experiment. *Bull. Am. Meteorol. Soc.* **79**, 2033–2058.

Melsheimer, C., Alpers, W. and Gade, M. 2001. Simultaneous observations of rain cells over the ocean by the synthetic aperture radar aboard the ERS satellites and by surface-based weather radars. *J. Geophys. Res. Oceans* **106**, 4665–4677.

Moore, G. W. K. 1985. The organization of convection in narrow cold-frontal rainbands. *J. Atmos. Sci.* **42**, 1777–1791.

Moore, G. W. K., Reader, M. C., York, J. and Sathiyamoorthy, S. 1996. Polar lows in the Labrador Sea – a case study. *Tellus A* **48A**, 17–40.

Moore, G. W. K. and Vachon, P. W. 2002. A polar low over The Labrador Sea: interactions with topography and an upper-level potential vorticity anomaly, and an observation by RADARSAT-1 SAR. *Geophys. Res. Lett.* **29**, 1773, DOI:10.1029/2001GL014007.

Moore, R. W. and Vonder Haar, T. H. 2003. Diagnosis of a polar low warm core utilizing the advanced microwave sounding unit. *Weather Forecast.* **18**, 700–711.

Mourad, P. D., Thompson, D. R. and Vandemark, D. C. 2000. Extracting fine-scale wind fields from synthetic aperture radar images of the ocean surface. *J. Hopkins APL Tech. D.* **21**, 108–115.

Pagowski, M. and Moore, G. W. K. 2001. A numerical study of an extreme cold-air outbreak over the Labrador Sea: sea ice, air-sea interaction, and development of polar lows. *Mon. Weather Rev.* **129**, 47–72.

Parish, T. R. 1983. The influence of the Antarctic Peninsula on the windfield over the western Weddell Sea. *J. Geophys. Res. Oceans Atmos.* **88**, 2684–2692.

Rasmussen, E. A., Claud, C. and Purdom, J. F. 1996. Labrador Sea polar lows. *Global Atmos. Ocean Syst.* **4**, 275–333.

Rasmussen, E. A. and Turner, J. 2003. *Polar Lows: Mesoscale Weather Systems in the Polar Regions* 1st Edition. Cambridge University Press, Cambridge, UK. pp. 612.

Renfrew, I. A., Moore, G. W. K., Guest, P. S. and Bumke, K. 2002. A comparison of surface layer and surface turbulent flux observations over the Labrador Sea with ECMWF analyses and NCEP reanalyses. *J. Phys. Oceanogr.* **32**, 383–400.

Renfrew, I. A., Moore, G. W. K., Holt, T. R., Chang, S. W. and Guest, P. 1999. Mesoscale forecasting during a field program: meteorological support of the Labrador Sea deep convection experiment. *Bull. Am. Meteorol. Soc.* 605–620.

Sanders, F. and Gyakum, J. R. 1980. Synoptic-dynamic climatology of the bomb. *Mon. Weather Rev.* **108**, 1589–1606.

Sikora, T. D., Friedman, K. S., Pichel, W. G. and Clemente-Colon, P. 2000. Synthetic aperture radar as a tool for investigating polar mesoscale cyclones. *Weather Forecast.* **15**, 745–758.

van den Broeke, M. R. and Gallee, H. 1996. Observation and simulation of barrier winds at the western margin of the Greenland ice sheet. *Q. J. R. Meteorol. Soc.* **122**, 1365–1383.

Wakimoto, R. M. and Bosart, B. L. 2000. Airborne radar observations of a cold front during FASTEX. *Mon. Weather Rev.* **128**, 2447–2470.

Wu, S. Y. and Liu, A. K. 2003. Towards an automated ocean feature detection, extraction and classification scheme for SAR imagery. *Int. J. Remote Sens.* **24**, 935–951.